THE JOURNAL OF PHYSICAL CHEMISTRY C
A JOURNAL OF THE AMERICAN CHEMICAL SOCIETY

pubs.acs.org/JPCC

Article

Imaging and Localization of Single Emitters near Plasmonic Particles of Different Size, Shape, and Material

Frank Bloksma and Peter Zijlstra*

Cite This: *J. Phys. Chem. C* 2021, 125, 22084−22092

Read Online

ACCESS | Metrics & More | Article Recommendations | Supporting Information

ABSTRACT: Colloidal plasmonic materials are increasingly used in biosensing and catalysis, which has sparked the use of super-resolution localization microscopy to visualize processes at the interface of the particles. We quantify the effect of particle−emitter coupling on super-resolution localization accuracy by simulating the point spread function (PSF) of single emitters near a plasmonic nanoparticle. Using a computationally inexpensive boundary element method, we investigate a broad range of conditions allowing us to compare the simulated localization accuracy to reported experimental results. We identify regimes where the PSF is not Gaussian anymore, resulting in large mislocalizations due to the appearance of multilobed PSFs. Such exotic PSFs occur when near-field excitation of quadrupole plasmons is efficient but unexpectedly also occur for large particle−emitter spacing where the coherent emission from the particle and emitter results in anisotropic emission patterns. We provide guidelines to enable faithful localization microscopy near colloidal plasmonic materials, which indicate that simply decreasing the coupling between particle and molecule is not sufficient for faithful super-resolution imaging.

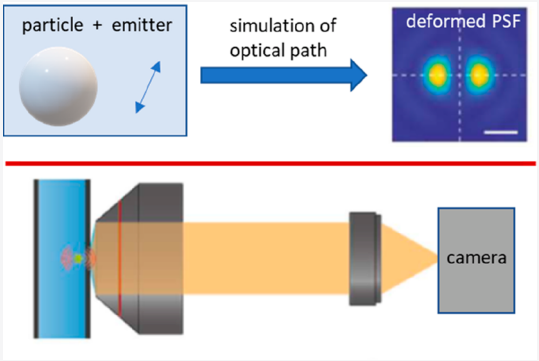

INTRODUCTION

Colloidal nanoparticles constitute materials with intermediate sizes between atoms and bulk materials, providing them with unique physicochemical properties. Colloidal materials are therefore increasingly used as biochemical probes and sensors. The colloid serves for example as an optical marker to visualize cellular structures,[1] as a carrier for targeted drug delivery,[2] or as a biosensor to enable single-molecule sensing.[3] For each of these applications, the particles are chemically functionalized to steer their interactions with their local environment. The chemical nature of the particle interface therefore dictates the behavior in the respective application, where for example the presence of functional groups determines the interaction with biomolecules and cell surface receptors.

The chemical interface of the particle is, however, inherently heterogeneous because the number and distribution of functional groups vary from particle to particle due to the random nature of functionalization protocols. Although particle-to-particle variations are inevitable, they are not revealed in commonly used characterization methods that use ensemble-averaging approaches, e.g., supernatant assays. Recently, super-resolution microscopy has emerged as a promising method to characterize the chemical interface of synthetic materials by using fluorescence imaging.[4−9] Herein single emitters are localized by using super-resolution microscopy, providing a direct visualization of the number and distribution of functional groups. Similarly, in the field of plasmon-mediated catalysis, super-resolution microscopy is increasingly used to quantify the distribution of catalytically active sites on the particle surface.[10,11]

Stochastic and deterministic super-resolution methods have been developed in the past decades that provide a spatial resolution (or localization precision) on the order of 10 nm, promising the visualization of the chemical interface with a precision far below the diffraction limit of light. In stochastic super-resolution microscopy, the point spread function (PSF) of a single emitter is fitted with an appropriate model to yield an estimate of its position.[12,13] This method works well for a freely rotating emitter in a homogeneous photonic environment, whose radiation pattern is isotropic resulting in an Airy disk on the detector.[14] However, contrary to biological systems such as vesicles and microtubules, a nearby particle introduces a fundamental challenge because it creates an anisotropic photonic environment. This may strongly affect the radiation pattern of an emitter, particularly for plasmonic particles where the emitter couples with the plasmonic modes of the particle.[15−22]

Received: July 27, 2021
Revised: September 20, 2021
Published: October 5, 2021

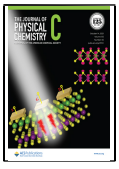

https://doi.org/10.1021/acs.jpcc.1c06665
J. Phys. Chem. C 2021, 125, 22084−22092

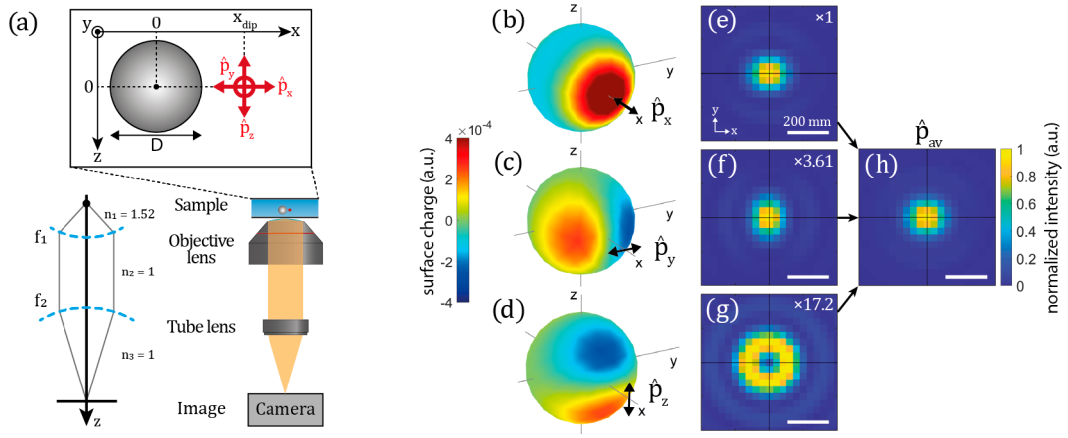

Figure 1. (a) Image formation of a dipole−emitter near a particle. The emission of the particle−emitter hybrid is collected and focused on the camera by using an objective and a tube lens with different focal lengths f_1 and f_2. The refractive indices before, between, and after the lenses is given by n_1, n_2, and n_3. The particle is located in the focal point of the objective lens (the origin of the coordinate system), and the dipole emitter is positioned along the x-axis at x_{dip} where three orthogonal dipole orientations $\hat{p}_x$, $\hat{p}_y$, and $\hat{p}_z$ are considered. (b−d) Calculated surface charge distributions on a 10 nm diameter silver sphere for $\hat{p}_x$, $\hat{p}_y$, and $\hat{p}_z$, respectively. The dipole is positioned 10 nm from the particle surface, and its emission is resonant with the plasmon at 405 nm. The colorbar indicates the charge on the particle surface and is shared for all dipole orientations. (e−g) Calculated PSFs corresponding to the particle−emitter hybrid in (b−d), where the color indicates the normalized intensity on the detector (normalization factor indicated). (h) Averaging over the PSFs in (e−g) yields the PSF for the orientation-averaged dipole $\hat{p}_{av}$.

Such coupling of the emitter to the plasmonic particle may enhance the fluorescence intensity and thereby increase the localization precision.[23,24] However, a shift between the position of the detected signal and the actual position of the emitter (the ground truth) decreases the accuracy of the localization. The origin of the decreased accuracy is the coherent interplay between the radiation from the emitter and the induced surface charge on the particle and their respective phase. The resulting total field at the detector is then often not dipolar anymore, resulting in a modified PSF in both shape and position. Such changes in directionality have been exploited to synthesize highly directional antennas made from particle assemblies.[25,26]

In the context of faithful super-resolution microscopy on particles, the problem has been studied by coupling emitters to silver and gold spheres,[18,21,22] triangles,[19] nanorods,[16,20,27] nanoislands,[18,28] nanowires,[15,17,29−31] and particle-on-film systems.[32] The modification of the PSF has further been explored from a theoretical point of view by using analytical approximations[33] or numerical simulations for spheres,[34] nanorods,[16] and triangles.[19] In some studies mislocalization was observed as a dominant effect,[16,18−22] other studies reported it to be negligible compared to the localization precision of the microscope,[4,35] and some studies reported exotic multilobed PSFs.[15,17] The variation in reported effects has its root largely in the different particle size, shape, and material used as well as the particle−emitter spacing and spectral detuning.

Here we present numerical simulations of the PSF of single emitters near a plasmonic nanoparticle to provide guidelines for faithful super-resolution localization microscopy on particles. We use a computationally inexpensive boundary element method (BEM) to compute the radiation pattern of particle−emitter hybrids and their PSF in an optical microscope. We study the shape and location of the PSF as a function of spectral overlap and particle−emitter spacing for the most commonly used colloidal gold and silver spheres and nanorods. We find regimes in which the mislocalization is much larger than expected due to asymmetric quadrupole-like emission patterns. Such exotic PSFs occur when near-field excitation of quadrupole plasmons is efficient but unexpectedly also occur for large particle−emitter spacing where the coherent emission from the particle and emitter results in anisotropic emission patterns. We provide guidelines to enable faithful localization microscopy near colloidal plasmonic materials, which indicate that simply decreasing the coupling between particle and molecule is not sufficient for faithful super-resolution imaging.

COMPUTATIONAL APPROACH

We focus on colloidal spheres and rods because these are most commonly employed in biosensing and drug targeting studies. For these nanostructures the super-resolution microscopy of the organization of surface ligands is relevant, whereas defects and polycrystallinity play a minor role in their optical properties. In the simulations we consider a dipolar emitter with a single emission wavelength in the presence of a nanoparticle (see Figure 1a). The particle is at the origin, whereas the emitter is placed anywhere in the xy-plane outside the particle. To simplify the model, we neglect the effect of the glass substrate by index matching the medium index with the glass (which due to symmetry has no effect on the shape of the PSF). We use a boundary element method (BEM) approach using the MNPBEM toolbox[36,37] where the emitter is represented as a point-like dipole excitation source. In contrast to analytical dipole approximations,[33] this full-wave approach takes into account both dipolar and higher-order modes in the particle.

The far-field radiation from the nanoparticle−emitter hybrid is then propagated through an imaging system and focused on a camera. The imaging process is simulated by calculating the electric fields that are refracted and focused by two lenses included in the optical setup and follows the geometrical optical theory as described by Novotny and Hecht.[14] Simulation parameters were chosen to represent an objective numerical aperture of 1.49 with a pixel size in the image plane of 33 nm.

https://doi.org/10.1021/acs.jpcc.1c06665
J. Phys. Chem. C 2021, 125, 22084−22092

We assume that the rotational diffusion of the dipole occurs on shorter times than the typical fluorescence lifetime. This is a reasonable assumption for e.g. small emitters attached via a floppy linker, whose rotations typically occur on subnanosecond time scales. In this case the excitation and emission processes are uncorrelated, allowing us to only consider the emission process in the form of an averaged dipole orientation $\hat{p}_{av}$ whose intensity $|\mathbf{E}|_{av}^2$ in the detector plane is given by

$$|\mathbf{E}|_{av}^2 = \frac{1}{3}[|\mathbf{E}|_x^2 + |\mathbf{E}|_y^2 + |\mathbf{E}|_z^2] \quad (1)$$

where $|\mathbf{E}|_{x,y,z}^2$ is the PSF for a dipole oriented along the x-, y-, and z-axis, respectively. Because the simulations do not suffer from any noise or background signal, we localize the apparent center of the PSF by calculating its center of mass. This provides a metric for the center of the detector image with no assumptions on the shape of the PSF as is usually the case for a Gaussian fit of the PSF. We explicitly indicate regimes where the PSF is asymmetric. We refer to the Supporting Information (Figures S1−S5) for a more detailed description and benchmarks of the simulations.

RESULTS AND DISCUSSION

To determine the effect of the particle on the image formation, we numerically calculate the far-field radiation for particle−emitter hybrids with varying dimensions, shapes, and materials. In Figure 1b−h the example is given for a 10 nm silver sphere (dipolar plasmon at λ_{SP} = 405 nm) where the emitter (a dipole emitting at 405 nm) is positioned 10 nm away from the particle surface in the xy-plane. As a result of the dipole excitation, mirror charges on the particle surface are formed whose distribution and magnitude depend on the orientation of the emitter's dipole moment, the particle−emitter spacing, and the detuning between emitter wavelength and particle plasmon. The latter also affects the relative phase between the charges on the dipole and the particle: taking the (approximate) analogy with a dispersion-less driven damped harmonic oscillator, the charges oscillate in-phase for far red-shifted dipoles and in quadrature for far blue-shifted dipoles.

The far-field radiation pattern then consists of coherent contributions originating from the emitter and from the induced charges on the particle, which interfere in the far-field and form an image on the camera. The corresponding PSF of the particle−emitter hybrid is shown for each dipole orientation in Figure 1e−g, while the PSF for the orientation-averaged case $\hat{p}_{av}$ is shown in Figure 1h. Note that $|\mathbf{E}|_z^2$ is much smaller than the other two contributions because in that case only a small part of the radiation is captured by the objective lens.

Depending on the relative magnitude and phase of the coherent contributions from the emitter and particle the radiation pattern is modified, and the resulting PSF on the camera is shifted away from the true dipole location. The total radiation pattern and thus the center of mass of the PSF therefore depend strongly on the spectral detuning (in units of the plasmon line width Γ) as is shown in Figure 2. The mislocalization is shown for the same 10 nm silver sphere for particle−dipole spacings along the x-axis ranging from 2 to 25 nm. This represents the typical range of spacings that is accessible if particles are coated with single-stranded DNA or polymeric brushes and for particle−emitter hybrids assembled on DNA origami platforms. Note that the PSF is only shifted along the x-axis due to the symmetry of the system; therefore, only the x-coordinate of the center of mass of the detector signal is plotted.

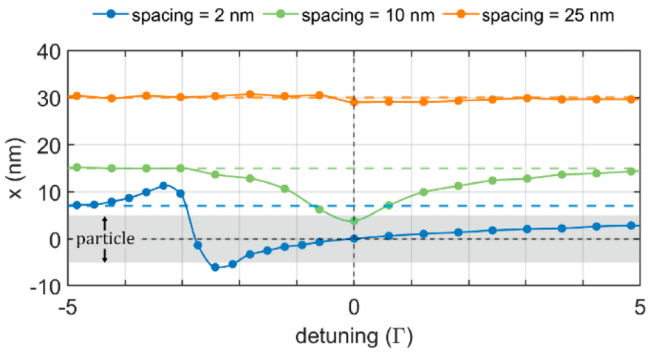

Figure 2. Calculated apparent center of mass of the detector signal (x-coordinate) of the emitter as a function of detuning for a 10 nm silver sphere and a 2 nm (blue), 10 nm (green), and 25 nm (orange) particle−dipole spacing. The true dipole positions are indicated with the horizontal dotted lines, and the extent of the particle is highlighted by the gray area.

For the 25 nm spacing we find that the PSF is accurately centered on the position of the emitter because the weak particle−emitter coupling results in negligible induced charge on the particle. For 10 nm spacing we find that the localization occurs closest to the particle center, i.e., x = 0, when the emitter is resonant with the plasmon, i.e., zero detuning. In this case the radiation pattern is dominated by the induced charges on the particle, resulting in a PSF that is nearly centered at the particle position. Increasing the detuning, the mislocalization reduces until the true emitter position is recovered. The effect of detuning is different for blue- or red-shifted emitters, which is a result of the coherent phase relation between the excitation dipole and induced charges that switches sign when crossing the resonance. This results in a switch from constructive to destructive interference, which we will get back to later.

For 2 nm spacing we find that the PSF is exactly centered on the position of the particle for zero detuning, indicating an emission pattern that is dominated by the induced charges on the particle. For red-shifted emitters the relative contribution of the emitter emission increases and the center of mass of the PSF slowly shifts back to the emitter position. In contrast, for detunings between −4Γ and −2Γ the center of mass of the detector signal switches from one side of the particle to the other. This dispersive behavior is not caused by deformation of the PSF; all PSFs were found to be near perfect Airy disks for the 10 nm silver spheres (see Figure 4g).

To elucidate the mechanism behind this dispersive behavior, we plot the data for the 2 nm spacing again in Figure 3a but for each dipole orientation, $\hat{p}_x$, $\hat{p}_y$, and $\hat{p}_z$ separately. We observe a complex behavior as a function of detuning. Starting at plasmon resonance (zero detuning), the total emission is localized at the particle center irrespective of the dipole orientation because the total radiated field is dominated by the particle. The latter can be seen in Figure 3b−d, where the emitted intensity averaged over the solid angle of the objective lens is displayed for the particle and emitter separately. Depending on the dipole orientation, for small detuning the field emitted by the particle is 5−10 times stronger than the emitter's field, resulting in a PSF whose center of mass represents the particle location.

For moderate detuning < |3Γ| it is clearly observed that the emissions from particle and dipole interfere constructively or

https://doi.org/10.1021/acs.jpcc.1c06665
J. Phys. Chem. C 2021, 125, 22084−22092

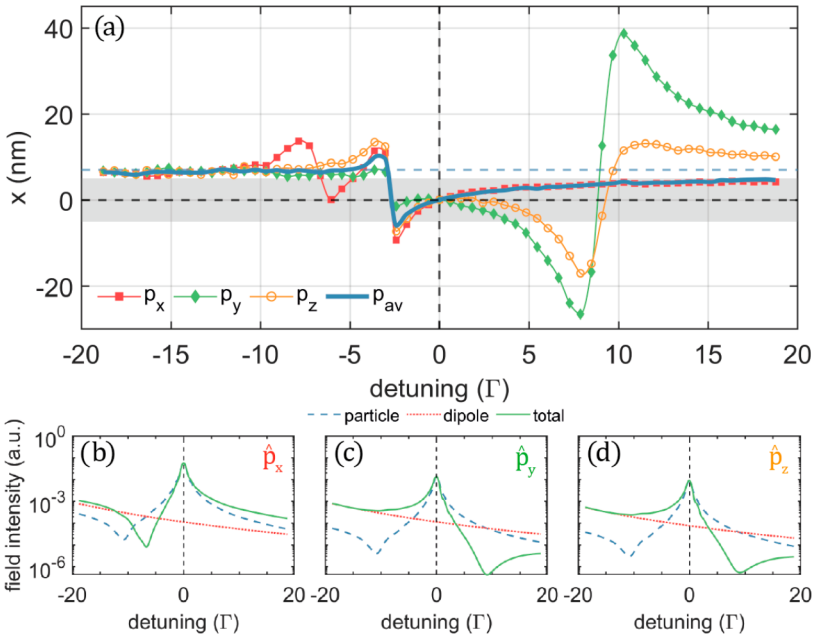

Figure 3. (a) Center of mass of the detector signal as a function of detuning for a 10 nm silver sphere and a 2 nm particle−emitter spacing. Results are plotted for three orthogonal dipole orientations, i.e., $\hat{p}_x$ (solid red squares), $\hat{p}_y$ (solid green diamonds), and $\hat{p}_z$ (open orange circles). The blue solid line indicates the center of mass for an orientation-averaged dipole $\hat{p}_{av}$. The true dipole position is indicated with the blue dashed line, and the range of coordinates occupied by the particle is highlighted by the gray area. (b−d) Electric field intensities (E^2) averaged over the solid angle of the objective lens as a function of detuning for $\hat{p}_x$, $\hat{p}_y$, and $\hat{p}_z$, respectively. The contributions of the particle and dipole fields are indicated by the blue dashed and red dotted lines, respectively. The total field intensity, resulting from the coherent addition of the particle and dipole fields, is given by the green lines.

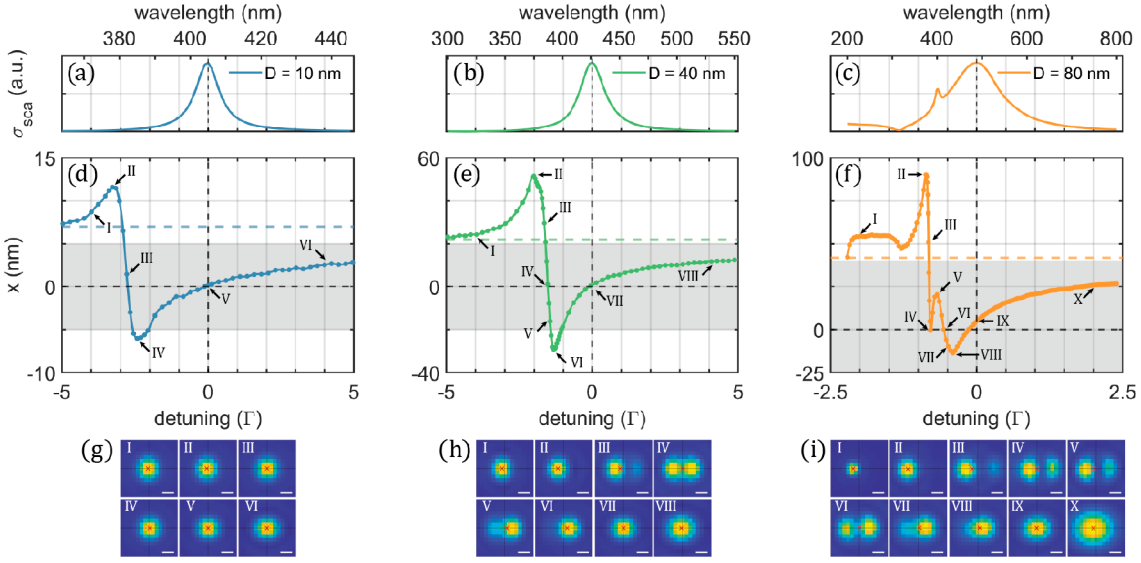

Figure 4. (a−c) Calculated scattering cross sections σ_{sca} for a 10, 40, and 80 nm diameter silver sphere, respectively. (d−f) Calculated center of mass of the detector signal x as a function of detuning for a 2 nm particle−dipole spacing. The true dipole positions are indicated with the colored horizontal dashed lines, and the particle dimensions are highlighted by the gray areas. (g−i) Calculated orientation-averaged PSFs corresponding to points in (d−f), respectively. The red cross shows the PSF's center of mass. Scale bars: 100 nm.

destructively depending on the dipole orientation and the detuning. In the case of a $\hat{p}_x$ dipole, where the dipole and the mirror charges are aligned end to end (Figure 1b), negative detuning induces out-of-phase oscillation between dipole and mirror charges, which results in destructive interference. This is evident in Figure 3b, where particularly around a detuning of −7Γ the field amplitudes of particle and dipole are in quadrature and similar in amplitude, resulting in a small contribution to the total field. Near this point, the total radiation pattern is asymmetric, and as a result the center of mass of the PSF exhibits dispersive behavior as can be seen for the $\hat{p}_x$ dipole in Figure 3a. The orientation-averaged PSF does not convey this behavior because the destructive interference results in a small contribution to the total detector signal.

A similar behavior is observed for $\hat{p}_y$ and $\hat{p}_z$ dipoles (Figure 3c,d), where we again observe dispersive behavior in the regime where the field amplitudes of particle and dipole are comparable. Now the regime in which destructive interference

https://doi.org/10.1021/acs.jpcc.1c06665
J. Phys. Chem. C 2021, 125, 22084−22092

occurs is however at a positive detuning of ∼9Γ because the dipole orientation is now parallel to the particle surface (Figure 1c,d). Revealing these orientation-dependent properties experimentally is challenging and will require emitters with a fixed orientation of their dipole moment with respect to the particle. This could be achieved by using e.g. quantum rods[38] or fluorophores with multiple anchors keeping them orientationally restricted.[39,40]

The only dispersive region that has a non-negligible contribution to the orientation-averaged detector signal is the feature we observe at a detuning of approximately −3Γ, which occurs for all dipole orientations. As can be seen in Figure 3b−d, the total radiation is dominated by the particle for all dipole orientations, where the relatively weak radiation of the dipole interferes destructively for the $\hat{p}_x$ dipole and constructively for the dipoles $\hat{p}_y$ and $\hat{p}_z$. Closer inspection of the surface charge distribution and radiation pattern of the particle (see Figure S6) indicates that its radiation resembles a tilted dipole-like pattern caused by an asymmetric charge distribution on the particle. Interestingly, the radiation pattern exhibits the same asymmetry for detunings of both −3.1Γ and −2.4Γ, even though the center of mass of the PSF shifts from one side of the particle to the other. This exemplifies that simple interpretation of the directionality of the radiation pattern is incomplete, and the underlying phase of the electric fields has to be taken into account.

The particle sizes in experimental studies vary greatly, so we now explore the size dependence in Figure 4. We show the calculated center of mass of the PSF for a 10, 40, and 80 nm silver sphere with a 2 nm particle−dipole spacing. In Figure 4a−c we show the numerically calculated scattering spectra of the particles under far-field excitation by a plane wave. The far-field spectra for the 10 and 40 nm particles exhibit a single dipolar resonance around 400 nm, whereas for the larger 80 nm particle a weak quadrupole mode becomes visible on the blue wing of the dipolar resonance.

In Figure 4d−f we plot the center of mass of the PSF for each particle−dipole system as a function of detuning. Each particle size exhibits a similar dispersive behavior for blue-shifted dipoles, where the center of mass of the PSF shifts from one side of the particle to the other. The 10 nm sphere was just discussed above, where we observed a switch of the center of mass of the PSF from one side of the particle to another, while the PSF remained near-Gaussian. For the 40 and 80 nm diameter spheres we observe a very different dispersive behavior that is not caused by the coherent addition of two (near) dipolar fields (one from the emitter and one from the particle) but is now caused by near-field excitation of a quadrupole mode on the particle. The quadrupole emission of the particle then interferes with the dipole's emission, resulting in an asymmetric multilobed PSF.

Inspecting the induced surface charge on the 40 and 80 nm particles confirms this (see Figure S7), where we observe an in-line quadrupolar charge distribution resulting in an asymmetric quadrupolar emission pattern. Note that for the larger particles the PSF center differs from the true dipole position for a larger range of emission wavelengths. This is the result of a broader plasmon resonance in combination with a stronger coupling to the particle, thereby requiring a larger detuning to sufficiently weaken the particle−emitter interaction for accurate localization.

Having established the basic mechanisms at play, we now turn our attention to a general description of mislocalization across the most commonly employed particle geometries. The aim of this description is to rationalize the various conditions reported in the literature and to provide design rules for future experiments to achieve faithful super-resolution localization microscopy. We investigate the mislocalization as a function of emitter detuning and particle−emitter spacing. We simulate particle−emitter spacings of 2−60 nm that cover the wide range of linkers used in experimental studies such as polyelectrolyte spacers and DNA.

For many applications gold is the preferred metal due to its chemical inertness, so we start in Figure 5 by comparing silver

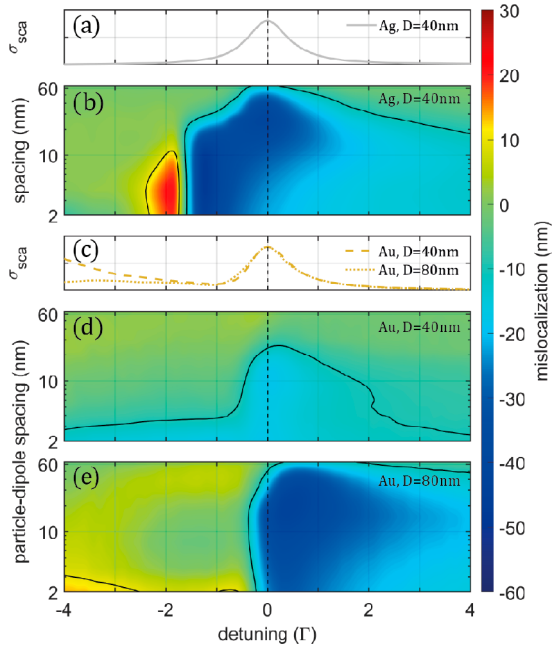

Figure 5. Mislocalization for emitters near gold and silver spheres. (a) Normalized scattering cross section of a 40 nm diameter silver sphere as a function of detuning from the plasmon resonance. (b) Contour plot of the mislocalization for the 40 nm silver sphere for different particle−dipole spacings in the *xy*-plane. A negative mislocalization indicates displacement of the PSFs center of mass in the direction of the particle. The black lines enclose regions where the mislocalization is larger than 10 nm, the localization precision of state-of-the-art instruments. (c) Normalized scattering cross section of a 40 and 80 nm diameter gold sphere as a function of detuning from their respective plasmon resonance. (d, e) Contour plot of the mislocalization for the gold spheres.

and gold spheres. Similar to what we have found previously, the PSF for both materials is displaced toward the particle center when the dipole is resonant with the plasmon (indicated by the blue shade in Figure 5). For the gold spheres a resonant emitter in close proximity to the particle exhibits a mislocalization that is roughly equal to the particle radius; in other words, the PSF is centered on the particle. As expected, for positive detuning the PSF slowly shifts back to the emitter position.

For blue-shifted emitters we observe stark differences between gold and silver. For silver (Figure 5b) we again observe a pronounced feature at approximately −2Γ which we attributed above to near-field excitation of an asymmetric quadrupole mode on the particle. This influence of the quadrupole mode is completely absent for both gold particle diameters. We attribute this to the fact that the quadrupole

https://doi.org/10.1021/acs.jpcc.1c06665
J. Phys. Chem. C 2021, 125, 22084−22092

mode for gold spheres is heavily damped by the interband transitions. This results in near-Gaussian (but displaced) PSFs for all spacings and detunings investigated.

The black contour lines in Figure 5 outline regions where the mislocalization is smaller than 10 nm, the typical localization precision of state-of-the-art instruments. For the 40 nm silver sphere the emitter has to be blue-shifted at least 2.5Γ from the plasmon resonance to minimize the effect of quadrupole emission. For red-shifted dipoles a considerable spacing is needed to minimize the particle-induced mislocalization, ranging from a minimal spacing of 15 nm at +5Γ to more than 60 nm at resonance. Because of smaller induced surface charges on the 40 and 80 nm gold sphere a substantially broader regime of negative detunings exists where mislocalization is negligible, implying that the choice of emitter in the case of a gold particle is less critical as long as it is blue-shifted from the plasmon resonance.

We now compare our simulations to experimental studies with the aim to rationalize the agreement between experiment and simulation for the various isolated conditions that have been reported in the literature. Starting with colloidal spheres (we will discuss gold nanorods later), several recent experiments reported measured mislocalizations.[21,22] Raab et al.[21] employed rectangular DNA origami structures that were designed to deterministically position a nearly resonant emitter (Cy3B) and a single gold sphere at a spacing of ∼10 nm. For 80 nm gold spheres they found a mislocalization of ∼20 nm along the optical axis in the direction of the particle. In this case the emitter and the particle were placed on an planar origami structure, resulting in an emitter that is not in the midplane of the particle as we considered here. The comparison with the current simulations is therefore indirect, but the magnitude of the shift of the PSF (about half the particle radius) is compatible with the results indicated in Figure 5e.

Fu et al.,[22] on the other hand, used 80 nm diameter gold particles in which the particle and a resonant dye were spaced by a double-stranded DNA linker. Because emitters were conjugated to the particle at random locations, the authors accumulated individual PSFs from many emitters aiming to reconstruct the geometry of the underlying particle. The reconstruction of each particle was then compared to numerical models. The data indicated a mislocalization of ∼40 nm toward the particle center irrespective of particle−emitter spacing up to 35 nm. This is in agreement with the numerical results presented in Figure 5e, where we considered emitters placed in the *xy*-plane only. The authors also compared their results, but their model took into account a 3D distribution of emitters around the particle. They found a detectable discrepancy between the measured and simulated mislocalization, which could indicate that the localizations were dominated by emitters near the *x*−*y*-plane with little contribution from emitters on the top and bottom of the particle. This highlights the need to measure the ground truth position for every emitter to enable faithful comparison to numerical models.

We now turn our attention to gold nanorods (GNR) which are widely used in applications ranging from biosensing to drug delivery and photothermal therapy. Driven by these applications, super-resolution localization of ligands on the particle surface has been presented by us and others.[4,16,35] Following these reports, we numerically investigated the PSF of an emitter near a GNR in Figure 6. We consider a 120 × 40 nm^2 spherically capped cylinder with a longitudinal and transverse plasmon resonance at 830 and 530 nm, respectively. The mislocalization is again plotted as a function of the detuning, which is now relative to the longitudinal plasmon of the particle (see Figure 6a). We consider two separate dipole positions: one near the tip and one near the side of the particle (see the insets in Figure 6b,c).

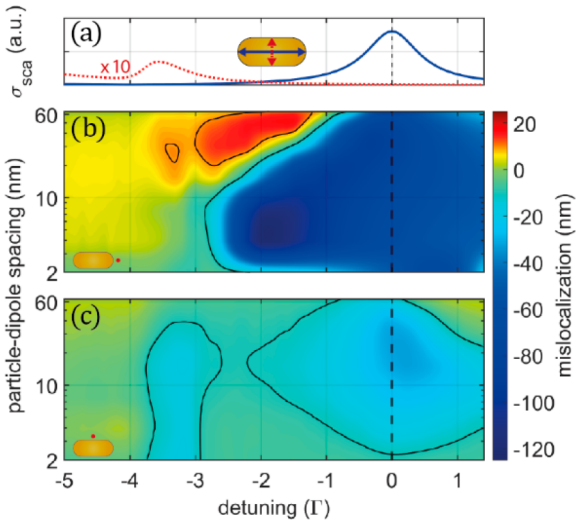

Figure 6. (a) Calculated scattering cross sections of a 120 × 40 nm^2 gold nanorod. The longitudinal and transverse modes are separately excited by using a plane wave with its polarization parallel to the long and short axes of the rod, respectively, as indicated by the double arrows in the cartoon. The cross section for the transverse mode is multiplied by 10 to increase visibility. (b, c) Calculated contour plots of the mislocalization as a function of detuning and particle−dipole spacing for a dipole position (b) near the tip and (c) near the side of the particle. The black lines enclose regions where the mislocalization is larger than 10 nm.

Starting with the dipole near the tip of the GNR (Figure 6b), we find that it interacts strongly with the longitudinal plasmon mode of the particle, resulting in regions of large mislocalization. As was the case for silver spheres the condition Γ = 0 results in near-perfect localization of the particle's center even for large particle−emitter spacings. For detuning below −3Γ we observe a regime where the mislocalization is smaller than the localization precision of a state-of-the-art instrument (indicated again by the black contours). Although the mislocalization is strongest for emitters that couple to the longitudinal plasmon, we find that coupling to the transverse plasmon also occurs. This is particularly the case for tip-positioned $\hat{p}_y$ and $\hat{p}_z$ dipoles that are aligned with one of the short axes of the GNR. Their contribution to the orientation-averaged PSF results in mislocalizations up to ∼10 nm even for particle−emitter spacings of several tens of nanometers (the yellow region in Figure 6b).

At specific combinations of detuning and spacing, we again observe the switching of negative to positive mislocalization. This behavior we found previously for silver spheres, but in that case this effect only occurred for short-ranged interactions. For emitters <10 nm from the silver particle an anisotropic quadrupolar plasmon was efficiently excited, resulting in a multilobed emission pattern. In contrast, here we observe a multilobed emission pattern for much larger particle−emitter spacings up to 60 nm. Inspecting the induced surface charge and radiation patterns (see Figure S8), we find that this is now

https://doi.org/10.1021/acs.jpcc.1c06665
J. Phys. Chem. C 2021, 125, 22084−22092

caused by the coherent addition of two end-to-end aligned dipoles (one from the particle and one from the emitter). This results in an anisotropic quadrupolar emission pattern when the field amplitude of both dipolar emission patterns is of similar magnitude. This also explains why this occurs only for specific combinations of detuning and particle−dipole spacing because it is at these specific combinations that the radiation field from the particle and emitter are of similar amplitude.

For an emitter along the short axis of the GNR (Figure 6c), however, we find only moderate mislocalizations that are concentrated around the longitudinal and transverse plasmon modes of the particle. Starting around $\Gamma = 0$, the $\hat{p}_x$ dipole (oriented along the long axis of the particle) couples weakly to the longitudinal plasmon, resulting in a moderate mislocalization that is maximized at a distance of several tens of nanometers from the particle. This indicates that up to several tens of nanometers of spacing the emitter is localized at the position of the particle center, leading to an increasing absolute mislocalization due to an increasing particle−emitter spacing. For detunings of approximately -3.5Γ the coupling of $\hat{p}_y$ and $\hat{p}_z$ dipoles to the transverse plasmon causes mislocalizations in slight excess of 10 nm, only just detectable by state-of-the-art instruments.

We now turn to experimental reports using colloidal gold nanorods, aiming to compare experimental results to the broad range of conditions simulated in Figure 6 (also see Figure S9). In all cases discussed below, the particle was coupled to many identical emitters to enable super-resolution reconstruction of the underlying particle geometry. Because colloidal gold nanorod samples typically exhibit a size distribution of at least 10%, the super-resolution reconstructions were compared to atomic force or electron microscopy images of the same particle. All authors used nanorods with sizes close to our simulations in Figure 6, so we neglect the effects of the residual differences in absolute particle size.

Blythe et al. used fluorophores with a small detuning of $-\Gamma$ and a particle−emitter spacing of several nanometers.[20,27] They consistently found an underestimation of the particle size, which is in good agreement with the simulations in Figure 6 that indicate a mislocalization of 20−40 nm toward the center of the particle. Su et al.[16] used resonant emitters and found that all point spread functions were centered on the particle, in agreement with a particle-dominated emission that results in localization of the particle center rather than the emitter. Taylor et al.,[4] on the other hand, used off-resonant emitters that transiently coupled to a gold nanorod using DNA hybridization. For a detuning of approximately -3Γ and a particle−emitter spacing of ∼7.5 nm, they estimated a mislocalization of <10 nm, in good agreement with Figure 6. Hamans et al.[10] mapped a catalytic reaction on the surface of a gold nanorod that generated a fluorescent product (resazurin) that gets trapped in an ∼16 nm thick silica shell encapsulating the particle. The product exhibited a detuning of -2Γ from the silica coated nanorods. Figure 6 predicts a sizable mislocalization under these conditions, but only for tip-bound emitters. The authors observed no substantial deviations in the reconstructed particle size, indicating that the reconstructions were dominated by side-bound emitters. Finally, De Silva Indrasekara et al.[35] and Saemisch et al.[41] investigated a range of spectral overlaps and particle−emitter spacings. Saemisch et al.[41] localized single molecules feely diffusing through the near-field of a gold nanorod and observed that the use of resonant antennas with a length of 150 nm resulted in the localization of the antenna center. When shortening the antenna to 115 nm (resulting in an approximate detuning of $+1\Gamma$ in the units of Figure 6), an approximate underestimation of the antenna length by ∼50 nm was observed, indicating a mislocalization of approximately −25 nm along the long axis of the particle. This is in qualitative agreement with Figure 6, where we note that the particle−emitter spacing was not controlled in the experiment. De Silva Indrasekara et al.[35] concluded that a particle−emitter spacing of ∼10 nm in combination with a detuning of $-\Gamma$ is needed to obtain faithful reconstruction. This seems contradictory to the results presented in Figure 6 because a detuning of $-\Gamma$ results in considerable mislocalization for tip-bound emitters. The faithfull reconstrunction of the particle size they found could be explained by a statistical underrepresentation of tip-conjugated emitters that would result in a mislocalization <10 nm for the side-bound emitters.

The simulation results indicate that the PSF can show strong deformation and exhibit a large mislocalization even when the emitter is weakly coupled to the plasmon resonance (i.e., for large particle−emitter spacing or for detuned emitters). This adds to the current understanding, where a large particle−emitter spacing in combination with spectral detuning is typically used to minimize mislocalization. This is sufficient to reduce the localization accuracy to a value close to the localization precision in some cases, but in the case of silver spheres and nanorods we also observed strong PSF deformation under these conditions. Because most experimental studies are concerned with 2D super-resolution localization, we have focused our simulations on emitters positioned in the *xy*-plane. In reality, the situation involves emitters at an arbitrary 3D location with respect to the particle. Understanding the full 3D geometry will require 3D super-resolution microscopy in combination with simulations in which the emitter is placed at an arbitrary 3D position. Importantly (and lacking in most experimental studies so far), a quantitative comparison to simulations will require knowledge about the ground-truth position of each emitter. This could be obtained from e.g. correlation with electron microscopy or atomic force microscopy. Furthermore, by fixing the orientation of the emitter, not only the effect of emitter location but also orientation could be studied to reveal polarization-dependent properties that are usually lost due to orientation averaging. Ideally, multimodal imaging may enable the collection of emission intensity, PSF shape,[17] fluorescence lifetime,[29] emission polarization,[42] and single-molecule spectra[43] to obtain a complete picture of particle−emitter coupling. Such experiments will shed light on the effect of a 3D photonic environment on optical imaging and will extend the realm of super-resolution microscopy to nano- and micrometer-sized colloids.

CONCLUSION

We simulated the PSF of a single emitter near a plasmonic nanoparticle to investigate the effect of particle−emitter coupling on the accuracy of super-resolution microscopy for different particle sizes, shapes, and materials. We show that the PSF is the result of coherent contributions originating from the emitter and induced mirror charges on the particle surface. In the limits of strong and weak interaction with the plasmon resonance (resulting in a PSF centered on the particle or the emitter, respectively), we find results that are in qualitative agreement with a range of experimental reports. We confirm that blue-shifting the dipole emission by several line widths

https://doi.org/10.1021/acs.jpcc.1c06665
J. Phys. Chem. C 2021, 125, 22084−22092

relative to the plasmon resonance reduces mislocalization to values below the accuracy of state-of-the-art instruments. In addition, we find regimes in which the mislocalization is much larger than expected due to multilobed quadrupole-like emission patterns. These regimes have not been investigated experimentally but already emerge for relatively small particles where asymmetric quadrupoles are excited by a closely spaced emitter and radiate efficiently into the far field. In addition, quadrupole-like emission and multilobed PSFs also occur due to an entirely different mechanism, namely the interference between dipolar emission patterns from particle and emitter. To facilitate faithful super-resolution localization on a range of particle shapes and sizes, we studied the mislocalization for gold and silver spheres and nanorods of different dimensions. For each particle type we find regimes where mislocalization is negligible, paving the way to use super-resolution localization microscopy as a method to characterize molecular binding and catalytic conversion on the surface of the particle.

■ ASSOCIATED CONTENT

Supporting Information

The Supporting Information is available free of charge at https://pubs.acs.org/doi/10.1021/acs.jpcc.1c06665.

Simulation details, benchmarks, localization algorithm, surface charge distributions, and schematic comparison between literature reports and simulations (PDF)

■ AUTHOR INFORMATION

Corresponding Author

Peter Zijlstra − *Department of Applied Physics & Institute for Complex Molecular Systems (ICMS), Eindhoven University of Technology, 5600 MB Eindhoven, The Netherlands;* orcid.org/0000-0001-9804-2265; Email: p.zijlstra@tue.nl

Author

Frank Bloksma − *Department of Applied Physics & Institute for Complex Molecular Systems (ICMS), Eindhoven University of Technology, 5600 MB Eindhoven, The Netherlands*

Complete contact information is available at: https://pubs.acs.org/10.1021/acs.jpcc.1c06665

Notes

The authors declare no competing financial interest.

■ ACKNOWLEDGMENTS

P.Z. acknowledges financial support from the SuperCol project that received funding from the European Union's Horizon2020 research and innovation program under the MarieSkłodowska-Curie Grant Agreement No. 860914.

■ REFERENCES

(1) Van Der Zwaag, D.; Vanparijs, N.; Wijnands, S.; De Rycke, R.; De Geest, B. G.; Albertazzi, L. Super Resolution Imaging of Nanoparticles Cellular Uptake and Trafficking. *ACS Appl. Mater. Interfaces* **2016**, *8*, 6391−6399.

(2) Wilhelm, S.; Tavares, A. J.; Dai, Q.; Ohta, S.; Audet, J.; Dvorak, H. F.; Chan, W. C. W. Analysis of Nanoparticle Delivery to Tumours. *Nat. Rev. Mater.* **2016**, *1*, 16014.

(3) Taylor, A. B.; Zijlstra, P. Single-Molecule Plasmon Sensing: Current Status and Future Prospects. *ACS Sensors* **2017**, *2*, 1103−1122.

(4) Taylor, A.; Verhoef, R.; Beuwer, M.; Wang, Y.; Zijlstra, P. All-Optical Imaging of Gold Nanoparticle Geometry Using Super-Resolution Microscopy. *J. Phys. Chem. C* **2018**, *122*, 2336−2342.

(5) Horáček, M.; Engels, D. J. D. J.; Zijlstra, P. Dynamic Single-Molecule Counting for the Quantification and Optimization of Nanoparticle Functionalization Protocols. *Nanoscale* **2020**, *12*, 4128−4136.

(6) Scheffold, F. Pathways and Challenges towards a Complete Characterization of Microgels. *Nat. Commun.* **2020**, *11*, 4315.

(7) Adelizzi, B.; Aloi, A.; Van Zee, N. J.; Palmans, A. R. A.; Meijer, E. W.; Voets, I. K. Painting Supramolecular Polymers in Organic Solvents by Super-Resolution Microscopy. *ACS Nano* **2018**, *12*, 4431−4439.

(8) Delcanale, P.; Miret-Ontiveros, B.; Arista-Romero, M.; Pujals, S.; Albertazzi, L. Nanoscale Mapping Functional Sites on Nanoparticles by Points Accumulation for Imaging in Nanoscale Topography (PAINT). *ACS Nano* **2018**, *12*, 7629−7637.

(9) Lubken, R. M.; De Jong, A. M.; Prins, M. W. J. How Reactivity Variability of Biofunctionalized Particles Is Determined by Super-positional Heterogeneities. *ACS Nano* **2021**, *15*, 1331−1341.

(10) Hamans, R. F.; Parente, M.; Baldi, A. Super-Resolution Mapping of a Chemical Reaction Driven by Plasmonic Near-Fields. *Nano Lett.* **2021**, *21*, 2149−2155.

(11) Zhou, X.; Andoy, N. M.; Liu, G.; Choudhary, E.; Han, K.-S.; Shen, H.; Chen, P. Quantitative Super-Resolution Imaging Uncovers Reactivity Patterns on Single Nanocatalysts. *Nat. Nanotechnol.* **2012**, *7*, 237−241.

(12) Mortensen, K. I.; Churchman, L. S.; Spudich, J. A.; Flyvbjerg, H. Optimized Localization Analysis for Single-Molecule Tracking and Super-Resolution Microscopy. *Nat. Methods* **2010**, *7*, 377−381.

(13) Deschout, H.; Cella Zanacchi, F.; Mlodzianoski, M.; Diaspro, A.; Bewersdorf, J.; Hess, S. T.; Braeckmans, K. Precisely and Accurately Localizing Single Emitters in Fluorescence Microscopy. *Nat. Methods* **2014**, *11*, 253−266.

(14) Novotny, L.; Hecht, B. *Principles of Nano-Optics*; Cambridge University Press: Cambridge, 2009.

(15) Su, L.; Lu, G.; Kenens, B.; Rocha, S.; Fron, E.; Yuan, H.; Chen, C.; Van Dorpe, P.; Roeffaers, M. B. J.; Mizuno, H.; et al. Visualization of Molecular Fluorescence Point Spread Functions via Remote Excitation Switching Fluorescence Microscopy. *Nat. Commun.* **2015**, *6*, 6287.

(16) Su, L.; Yuan, H.; Lu, G.; Rocha, S.; Orrit, M.; Hofkens, J.; Uji-I, H. Super-Resolution Localization and Defocused Fluorescence Microscopy on Resonantly Coupled Single-Molecule, Single-Nanorod Hybrids. *ACS Nano* **2016**, *10*, 2455−2466.

(17) Baiyasi, R.; Jebeli, S. A. H.; Zhang, Q.; Su, L.; Hofkens, J.; Uji-I, H.; Link, S.; Landes, C. F. PSF Distortion in Dye-Plasmonic Nanomaterial Interactions: Friend or Foe? *ACS Photonics* **2019**, *6*, 699−708.

(18) Wertz, E.; Isaacoff, B. P.; Flynn, J. D.; Biteen, J. S. Single-Molecule Super-Resolution Microscopy Reveals How Light Couples to a Plasmonic Nanoantenna on the Nanometer Scale. *Nano Lett.* **2015**, *15*, 2662−2670.

(19) Wertz, E. A.; Isaacoff, B. P.; Biteen, J. S. Wavelength-Dependent Super-Resolution Images of Dye Molecules Coupled to Plasmonic Nanotriangles. *ACS Photonics* **2016**, *3*, 1733−1740.

(20) Blythe, K. L.; Willets, K. A. Super-Resolution Imaging of Fluorophore-Labeled DNA Bound to Gold Nanoparticles: A Single-Molecule, Single-Particle Approach. *J. Phys. Chem. C* **2016**, *120*, 803−815.

(21) Raab, M.; Vietz, C.; Stefani, F. D.; Acuna, G. P.; Tinnefeld, P. Shifting Molecular Localization by Plasmonic Coupling in a Single-Molecule Mirage. *Nat. Commun.* **2017**, *8*, 13966.

(22) Fu, B.; Isaacoff, B. P.; Biteen, J. S. Super-Resolving the Actual Position of Single Fluorescent Molecules Coupled to a Plasmonic Nanoantenna. *ACS Nano* **2017**, *11*, 8978−8987.

(23) Chattopadhyay, S.; Biteen, J. S. Super-Resolution Characterization of Heterogeneous Light-Matter Interactions between Single

Dye Molecules and Plasmonic Nanoparticles. *Anal. Chem.* **2021**, *93*, 430−444.
(24) Willets, K. A.; Wilson, A. J.; Sundaresan, V.; Joshi, P. B. Super-Resolution Imaging and Plasmonics. *Chem. Rev.* **2017**, *117*, 7538−7582.
(25) Curto, A. G.; Volpe, G.; Taminiau, T. H.; Kreuzer, M. P.; Quidant, R.; van Hulst, N. F. Unidirectional Emission of a Quantum Dot Coupled to a Nanoantenna. *Science* **2010**, *329*, 930−933.
(26) Vecchi, G.; Giannini, V.; Gómez Rivas, J. Shaping the Fluorescent Emission by Lattice Resonances in Plasmonic Crystals of Nanoantennas. *Phys. Rev. Lett.* **2009**, *102*, 146807.
(27) Blythe, K. L.; Titus, E. J.; Willets, K. A. Triplet-State-Mediated Super-Resolution Imaging of Fluorophore-Labeled Gold Nanorods. *ChemPhysChem* **2014**, *15*, 784−793.
(28) Mack, D. L.; Cortés, E.; Giannini, V.; Török, P.; Roschuk, T.; Maier, S. A. Decoupling Absorption and Emission Processes in Super-Resolution Localization of Emitters in a Plasmonic Hotspot. *Nat. Commun.* **2017**, *8*, 14513.
(29) Blanquer, G.; Van Dam, B.; Gulinatti, A.; Acconcia, G.; De Wilde, Y.; Izeddin, I.; Krachmalnicoff, V. Relocating Single Molecules in Super-Resolved Fluorescence Lifetime Images near a Plasmonic Nanostructure. *ACS Photonics* **2020**, *7*, 393−400.
(30) Lin, H.; Centeno, S. P.; Su, L.; Kenens, B.; Rocha, S.; Sliwa, M.; Hofkens, J.; Uji-I, H. Mapping of Surface-Enhanced Fluorescence on Metal Nanoparticles Using Super-Resolution Photoactivation Localization Microscopy. *ChemPhysChem* **2012**, *13*, 973−981.
(31) Ropp, C.; Cummins, Z.; Nah, S.; Fourkas, J. T.; Shapiro, B.; Waks, E. Nanoscale Imaging and Spontaneous Emission Control with a Single Nano-Positioned Quantum Dot. *Nat. Commun.* **2013**, *4*, 1447.
(32) Horton, M. J.; Ojambati, O. S.; Chikkaraddy, R.; Deacon, W. M.; Kongsuwan, N.; Demetriadou, A.; Hess, O.; Baumberg, J. J. Nanoscopy through a Plasmonic Nanolens. *Proc. Natl. Acad. Sci. U. S. A.* **2020**, *117*, 2275−2281.
(33) Goldwyn, H. J.; Smith, K. C.; Busche, J. A.; Masiello, D. J. Mislocalization in Plasmon-Enhanced Single-Molecule Fluorescence Microscopy as a Dynamical Young's Interferometer. *ACS Photonics* **2018**, *5*, 3141−3151.
(34) Heaps, C. W.; Schatz, G. C. Modeling Super-Resolution SERS Using a T-Matrix Method to Elucidate Molecule-Nanoparticle Coupling and the Origins of Localization Errors. *J. Chem. Phys.* **2017**, *146*, 224201.
(35) De Silva Indrasekara, A. S.; Shuang, B.; Hollenhorst, F.; Hoener, B. S.; Hoggard, A.; Chen, S.; Villarreal, E.; Cai, Y. Y.; Kisley, L.; Derry, P. J.; et al. Optimization of Spectral and Spatial Conditions to Improve Super-Resolution Imaging of Plasmonic Nanoparticles. *J. Phys. Chem. Lett.* **2017**, *8*, 299−306.
(36) Hohenester, U.; Trügler, A. MNPBEM - A Matlab Toolbox for the Simulation of Plasmonic Nanoparticles. *Comput. Phys. Commun.* **2012**, *183*, 370−381.
(37) Waxenegger, J.; Trügler, A.; Hohenester, U. Plasmonics Simulations with the MNPBEM Toolbox: Consideration of Substrates and Layer Structures. *Comput. Phys. Commun.* **2015**, *193*, 138−150.
(38) Hu, J.; Li, L. S.; Yang, W.; Manna, L.; Wang, L. W.; Alivisatos, A. P. Linearly Polarized Emission from Colloidal Semiconductor Quantum Rods. *Science* **2001**, *292*, 2060−2063.
(39) Mathur, D.; Kim, Y. C.; Díaz, S. A.; Cunningham, P. D.; Rolczynski, B. S.; Ancona, M. G.; Medintz, I. L.; Melinger, J. S. Can a DNA Origami Structure Constrain the Position and Orientation of an Attached Dye Molecule? *J. Phys. Chem. C* **2021**, *125*, 1509−1522.
(40) Mortensen, K. I.; Sung, J.; Flyvbjerg, H.; Spudich, J. A. Optimized Measurements of Separations and Angles between Intra-Molecular Fluorescent Markers. *Nat. Commun.* **2015**, *6*, 8621.
(41) Saemisch, L.; Liebel, M.; Van Hulst, N. F. Isolating Strong Nanoantenna-Molecule Interactions by Ensemble-Level Single-Molecule Detection. *Nanoscale* **2020**, *12*, 3723−3730.
(42) Zuo, T.; Goldwyn, H. J.; Isaacoff, B. P.; Masiello, D. J.; Biteen, J. S. Rotation of Single-Molecule Emission Polarization by Plasmonic Nanorods. *J. Phys. Chem. Lett.* **2019**, *10*, 5047−5054.
(43) Saemisch, L.; Liebel, M.; van Hulst, N. F. Control of Vibronic Transition Rates by Resonant Single-Molecule-Nanoantenna Coupling. *Nano Lett.* **2020**, *20*, 4537−4542.

https://doi.org/10.1021/acs.jpcc.1c06665
J. Phys. Chem. C 2021, 125, 22084−22092